Journal of Materials Chemistry A

PAPER

View Article Online
View Journal | View Issue

Published on 02 November 2015. Downloaded by Technische Informationsbibliothek (TIB) on 02/12/2016 07:36:39.

Cite this: J. Mater. Chem. A, 2015, 3, 24008

Novel CO_2-tolerant Al-containing membranes for high-temperature oxygen separation

Kaveh Partovi,* Michael Bittner and Jürgen Caro

Received 16th June 2015
Accepted 2nd November 2015

DOI: 10.1039/c5ta04405g

www.rsc.org/MaterialsA

Novel dual-phase oxygen-transporting membranes with compositions 40 wt% $Nd_{0.6}Sr_{0.4}Al_{0.2}Fe_{0.8}O_{3-\delta}$–60 wt% $Ce_{0.9}Nd_{0.1}O_{2-\delta}$ (NSAF6428–CN91) and 40 wt% $Nd_{0.5}Sr_{0.5}Al_{0.2}Fe_{0.8}O_{3-\delta}$–60 wt% $Ce_{0.8}Nd_{0.2}O_{2-\delta}$ (NSAF5528–CN82) were successfully synthesized *via* a one-pot sol–gel method. The oxygen permeation performance and the structural properties of the membranes could be simultaneously improved owing to Al doping of the perovskite phase. The newly developed dense ceramic membranes (0.6 mm thick) displayed long-term stable oxygen permeation fluxes of 0.31 and 0.51 $cm^3\ min^{-1}\ cm^{-2}$ under an air/CO_2 oxygen partial pressure gradient at 950 °C for NSAF6428–CN91 and NSAF5528–CN82, respectively. The NSAF6428–CN91 showed a stable oxygen flux of 0.15 $cm^3\ min^{-1}\ cm^{-2}$ at 900 °C for 100 h, without any deterioration of the microstructure under pure CO_2 sweeping.

Introduction

Oxygen-transporting membranes (OTMs) based on mixed ionic–electronic conducting oxides (MIECs) have been extensively studied for a wide variety of applications, such as oxygen separation from air,[1–3] as membrane reactors for the conversion of hydrocarbons to value-added products,[4–8] or as cathode materials for solid oxide fuel cells.[9,10] In recent years, OTMs have attracted increasing attention for the application in power plants adopting oxyfuel concept for CO_2 capture, as a cost-efficient replacement for the traditional cryogenic air separation units.[11–13] The oxyfuel concept is based on utilization of high-purity oxygen instead of air for fuel combustion in power plants, thus facilitating carbon capture and storage (CCS) and minimizing the NO_x emissions. In order to control the combustion flame temperature, the combustion gas is partly diluted with the effluent CO_2. Therefore, the candidate MIECs for the oxyfuel concept should meet at least two main requirements: high oxygen permeability and good thermochemical stability against CO_2 and other corrosive gases, such as SO_2, as well as reducing agents such as methane.[14–16] However, the most promising MIECs in terms of oxygen permeability are single phase perovskite-type oxides, mainly $Ba_{1-x}Sr_xCo_{1-y}Fe_yO_{3-\delta}$ and $Ln_{1-x}Sr_xCo_{1-y}Fe_yO_{3-\delta}$ (Ln = La, Pr, Sm, *etc.*), containing alkaline earth metals Ba and Sr at the A-site of the perovskite structure ABO_3 and Co at the perovskite's B-site.[17–22] The presence of A-site Ba and Sr leads to the degradation of the membrane permeation performance in CO_2-rich environments, due to formation of $BaCO_3$ and $SrCO_3$ on the CO_2-exposed outer surface layer of the membrane, thus inhibiting the oxygen surface exchange reaction.[23–26]

The concept of dual-phase composite materials was developed to enhance the thermochemical stability and mechanical properties of the single-phase perovskite-type OTMs. $SmMn_{0.5}Co_{0.5}O_3$–$Ce_{0.8}Sm_{0.2}O_{1.9}$,[27] $La_{0.9}Sr_{0.1}FeO_{3-\delta}$–$Ce_{0.8}Sm_{0.2}O_{2-\delta}$,[28] $Pr_{0.6}Sr_{0.4}FeO_{3-\delta}$–$Ce_{0.9}Pr_{0.1}O_{2-\delta}$,[29] and $Pr_{0.6}Sr_{0.4}Co_{0.5}Fe_{0.5}O_{3-\delta}$–$Ce_{0.9}Pr_{0.1}O_{2-\delta}$,[30] are some examples of dual-phase compositions based on an ionic conducting fluorite-type phase, mainly doped ceria, and a mixed-conducting phase, such as perovskite oxides. However, despite their improved stability in CO_2-containing environments, dual-phase membranes exhibit lower oxygen permeability compared to single-phase membranes.

Recently, a CO_2-stable reduction-tolerant dual-phase material with the composition 40 wt% $Nd_{0.6}Sr_{0.4}FeO_{3-\delta}$–60 wt% $Ce_{0.9}Nd_{0.1}O_{2-\delta}$ (abbreviated as NSF64–CN91) was developed by our group.[31] Incorporation of Al at the B-site of the perovskite phase has been previously reported to increase the thermochemical stability of the membranes, also under reducing atmospheres,[32,33] correlating with reduced chemical and thermal expansion coefficients.[34,35] In this paper, we report enhanced oxygen permeability and structural improvement of NSF64–CN91 by partial substitution of Fe for Al at the B-site of the perovskite phase. Furthermore, the effect of higher Sr content and increased Nd doping of the fluorite phase on the CO_2 stability and oxygen permeability of the newly developed membranes 40 wt% $Nd_{0.6}Sr_{0.4}Al_{0.2}Fe_{0.8}O_{3-\delta}$–60 wt% $Ce_{0.9}Nd_{0.1}O_{2-\delta}$ (NSAF6428–CN91) and 40 wt% $Nd_{0.5}Sr_{0.5}Al_{0.2}Fe_{0.8}O_{3-\delta}$–60 wt% $Ce_{0.8}Nd_{0.2}O_{2-\delta}$ (NSAF5528–CN82) are investigated.

Experimental

The dual-phase materials with compositions of 40 wt% $Nd_{0.6}Sr_{0.4}Al_{0.2}Fe_{0.8}O_{3-\delta}$–60 wt% $Ce_{0.9}Nd_{0.1}O_{2-\delta}$ (abbreviated as NSAF6428–CN91) and 40 wt% $Nd_{0.5}Sr_{0.5}Al_{0.2}Fe_{0.8}O_{3-\delta}$–60 wt%

Institute of Physical Chemistry and Electrochemistry, Leibniz University of Hannover, Callinstr. 3a, D-30167 Hannover, Germany. E-mail: kaveh.partovi@pci.uni-hannover.de

This journal is © The Royal Society of Chemistry 2015

Published on 02 November 2015. Downloaded by Technische Informationsbibliothek (TIB) on 02/12/2016 07:36:39.

$Ce_{0.8}Nd_{0.2}O_{2-\delta}$ (abbreviated as NSAF5528–CN82) were synthesized *via* a one-pot sol–gel procedure, by mixing stoichiometric amounts of aqueous solutions of the related metal nitrates with ethylenediamine tetraacetic acid (EDTA) and citric acid (CA) to obtain a total metal cation/EDTA/CA ratio of 1 : 1 : 1.5. Ammonia solution was added to the mixture to maintain an approximate pH value of 9. The powder samples were obtained from the precursor after an evaporation procedure, elaborately described elsewhere.[36] Further details on the mechanisms involved in the one-pot sol–gel synthesis of the perovskites and the related dual-phase compositions are provided in the literature.[37–39] The ground sample powder were uniaxially pressed under a pressure of ~120 MPa into green disks (18 mm in diameter) and sintered in ambient air at 1400 °C for 5 h with heating/cooling rates of 2 °C min^{-1} to obtain 0.6 mm thick gas-tight membranes (16 mm in diameter).

X-ray diffraction (XRD) was applied to determine the phase structure of the membranes. The XRD measurements were conducted at room temperature in ambient air on a Bruker-AXS D8 Advance diffractometer with Cu-Kα radiation in a step-scan mode in the 2θ range of 20–80° at intervals of 0.02°. Rietveld refinement of the XRD data was conducted using TOPAS 4.2 software.

The electrical conductivity measurements were performed on sample bars (0.6 mm × 1.0 mm × 10 mm), cut out of the sintered material in the temperature range of 30 to 1000 °C with heating/cooling rates of 3 °C min^{-1} in a self-made cell in ambient air. The temperature-dependent DC conductivities were recorded on Keithley 2100 6-$\frac{1}{2}$ Digit multimeters, with Pt wires building a four-point probe geometry.

The microstructures and the phase compositions of the membranes were investigated by scanning electron microscopy (SEM) and back-scattered electron microscopy (BSEM) on a field-emission electron microscope of the type JEOL JSM 6700 F at excitation voltages of 2 kV and 20 kV, respectively. The elemental distribution of the composite materials was analyzed using energy-dispersive X-ray spectroscopy (EDXS) by a spectrometer (Model INCA A-300, Oxford Instruments) at the voltage of 20 kV.

Thermogravimetric and differential thermal analysis (TGA/DTA) were performed on the ground powder samples on a Setaram Setsys Evolution 1750 thermoanalyzer in the temperature range of 50 °C to 1000 °C with heating/cooling rates of 10 °C min^{-1} using synthetic air at a flow rate of 20 cm^3 min^{-1} as the purge gas.

For the oxygen permeation measurements, the membranes were fixed onto an alumina tube using gold cermet (conduction paste C5754, Heraeus, Hanau, Germany) and placed in a high-temperature permeation cell, described in detail elsewhere.[40] The permeation cell was placed in the center of a vertical tubular oven, while the dwelling temperatures were controlled by a K-type thermocouple positioned close to the membrane's surface. Synthetic air, consisting of 20 vol% O_2 and 80 vol% N_2 at a flow rate of 150 cm^3 min^{-1} was fed to the feed side of the membrane, while the permeation side of the membrane was swept with 49 cm^3 min^{-1} He (Linde, 99.996%) or CO_2 (Linde, 99.5%) and 1 cm^3 min^{-1} Ne (Linde, 99.995%), as the internal standard gas to calculate the total flow rate of the effluent gas mixture. The flow rates of the inlet gases were regulated by mass flow controllers (MFC, Bronkhorst, Ruurlo, The Netherlands). The total flow rate of the effluent was also measured using a soap-film flow meter. The composition of the effluent was quantitatively analyzed using gas chromatography (GC) on an online-coupled Agilent 6890A gas chromatograph equipped with a Carboxen-1000 column (Supelco). Possible oxygen leakage due to imperfections in the membrane sealing was calculated by monitoring the N_2 concentration in the effluent and was subtracted from the total O_2 flux, despite being negligible (<1% O_2 leakage) during the entire measurements.

Results and discussion

Phase structure and microstructure

As presented in Fig. 1, the room-temperature XRD patterns of the freshly sintered NSF–CN and NSAF–CN membranes could verify the two-phase composition of the membranes, consisting of the perovskite-type NSF or NSAF phase and the cubic fluorite-type phase (space group 225: $Fm\bar{3}m$) related to Nd-doped ceria (CN). The acquired XRD data revealed no additional phases. As previously reported by our group,[31] the perovskite NSF possesses an orthorhombic distorted symmetry (space group 74: *Imma*) at room temperature, which was also maintained up to 1000 °C according to the *in situ* XRD measurements. However, the XRD analysis revealed that the newly developed NSAF6428 and NSAF5528 perovskites possessed a cubic perovskite symmetry (space group 221: $Pm\bar{3}m$) even at room temperature, due to the partial substitution of Fe cation at the B-site of the perovskite structure for the slightly smaller Al

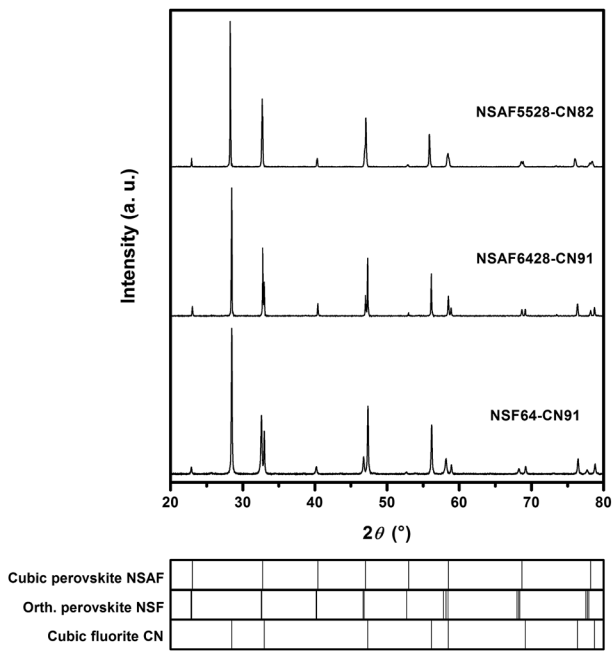

Fig. 1 Room temperature XRD patterns of the sintered dual-phase membranes with the main reflection positions of the constituent perovskite and fluorite-type phases.

Published on 02 November 2015. Downloaded by Technische Informationsbibliothek (TIB) on 02/12/2016 07:36:39.

cation. The ionic radii of the 6-fold coordinated B-site species are listed in Table 1.

In the case of NSF, the tilting of the BO_6 octahedra occurs due to the smaller cation size of Nd, resulting in an orthorhombic distortion of the perovskite structure. The trend of increasing orthorhombic distortion with decreasing A-site cation size has been previously reported for $LnNiO_3$ (Ln = La, Pr, Nd, Sm) perovskites,[41] which can also be represented as a negative deviation of the Goldschmidt's tolerance factor t from unity:[42]

$$t = \frac{r_A + r_O}{\sqrt{2}\,(r_B + r_O)} \quad (1)$$

where r_A, r_B, and r_O refer to the ionic radii of the A-site cation, B-site cation and oxygen, respectively. Thus, partial substitution of the larger Fe cation for the smaller Al cation is expected to have slightly increased the tolerance factor, resulting in a cubic perovskite structure, which facilitates the isotropic bulk diffusion of oxygen ion. Furthermore, a small shift of the NSAF perovskite's main reflection position towards higher diffraction angles compared to that of the NSF perovskite, confirms a slight shrinkage of the perovskite's unit cell, due to partial substitution of Fe for Al. Table 2 lists the calculated unit cell parameters of the sintered dual-phase membranes at room temperature.

Electrical conductivity

Fig. 2 shows temperature-dependent total electrical conductivity of NSF64–CN91, NSAF6428–CN91, and NSAF5528–CN82 compositions measured by a DC four-probe method in ambient air. The total electrical conductivity in mixed ionic–electronic conducting perovskite-type oxides, such as NSF and NSAF, can principally be attributed to the electronic conductivity, which is two orders of magnitude higher than the ionic conductivity. The electronic conduction is mediated by a thermally activated small-polaron hopping mechanism over B–O–B conduction pairs, consisting of overlapped 3d-orbitals of the B-site transition metal cations and the 2p-orbitals of the oxygen ion.[44,45] As can be seen in Fig. 2, the electronic conductivity of the compositions increases with increasing temperature to a maximum at T_{max}, indicating a semi-conductor behavior. Above this temperature the electronic conductivity decreases with increasing temperature, corresponding to the onset of oxygen release from the lattice. The decrease in electronic conduction above T_{max} results from increasing concentration of oxygen vacancies, as well as decreasing concentration of charge carriers.[46,47]

Table 1 Ionic radii of the 6-fold coordinated B-site species of the NSAF perovskite phase[43]

Cation	Radius (Å)
Al^{3+}	0.535
Fe^{3+} (HS)[a]	0.645
Fe^{3+} (LS)[b]	0.55
Fe^{4+}	0.585

[a] High spin. [b] Low spin.

Table 2 Calculated lattice parameters of the related phase components after sintering

Phase component	Crystal symmetry	a (Å)	b (Å)	c (Å)
NSF	Orthorhombic (*Imma*)	5.492	7.766	5.497
NSAF6428	Cubic ($Pm\bar{3}m$)	3.864	—	—
NSAF5528	Cubic ($Pm\bar{3}m$)	3.867	—	—
CN91	Cubic ($Fm\bar{3}m$)	5.438	—	—
CN82	Cubic ($Fm\bar{3}m$)	5.454	—	—

Accordingly, upon introduction of 20 at% Al^{3+} to the B-site of the perovskite phase in NSF64–CN91, lower conductivities are observed for NSAF6428–CN91 as the concentration of mixed-valence Fe^{3+}/Fe^{4+} is decreased, which is consistent with previous studies.[48,49]

Furthermore, increasing the concentration of the acceptor dopant Sr^{2+} at the A-site of the perovskite in NSAF6428–CN91 results in higher concentration of p-type charge carriers.[50] Consequently, higher conductivities are observed for

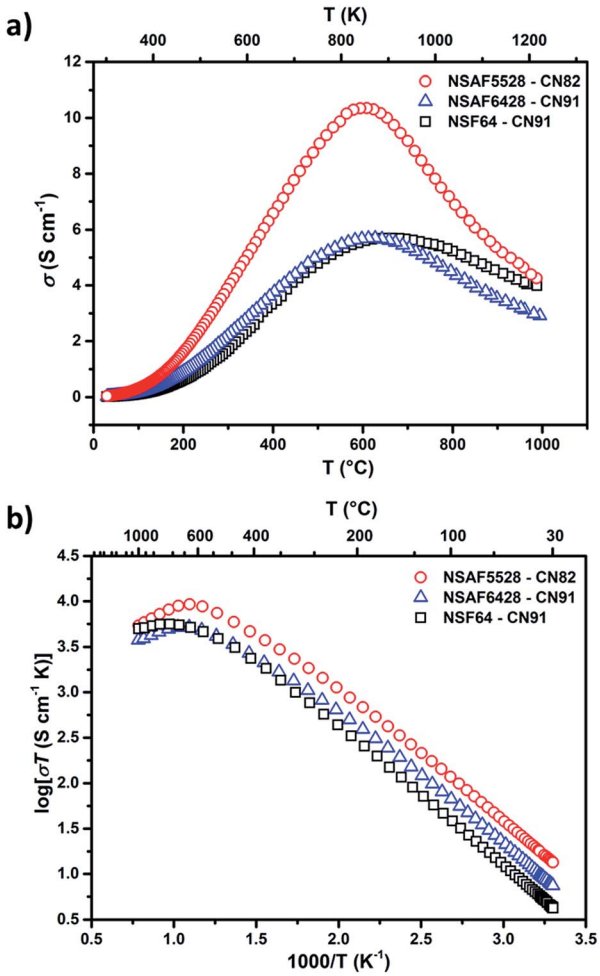

Fig. 2 Electrical conductivities of NSF64–CN91, NSAF6428–CN91, and NSAF5528–CN82 in air: (a) as a function of temperature, (b) represented as Arrhenius plots.

This journal is © The Royal Society of Chemistry 2015

Published on 02 November 2015. Downloaded by Technische Informationsbibliothek (TIB) on 02/12/2016 07:36:39.

NSAF5528–CN82, compared to NSF64–CN91 and NSAF6428–CN91. However, due to increased loss of oxygen above T_{max} a faster trend of decreasing conductivity is also observed for NSAF5528–CN82.

Membrane microstructure

The surface microstructure and elemental distribution of the membranes were studied by SEM and EDXS analysis. The SEM, BSEM and EDXS images of the sintered NSAF6428–CN91 and NSAF5528–CN82 are presented in Fig. 3 and 4, respectively. The SEM micrographs of the membrane surface show densely packed grains (Fig. 3a and 4a). The membrane surface was free of cracks and no additional particles could be observed. As can be seen in the BSEM images of the same spots (Fig. 3b and 4b), the grains of the perovskite phase NSAF (dark grains) and the fluorite phase CN (light grains) are uniformly distributed. The percolation network formed by the two phases can be more clearly observed in the EDXS mapping images showing separate Fe-rich (Fig. 3c and 4c) and Ce-rich (Fig. 3d and 4d) phases, corresponding to the perovskite and fluorite grains, respectively.

Oxygen permeation performance

Oxygen permeation performance of the dual-phase membranes NSAF6428–CN91 and NSAF5528–CN82 was studied using pure He and pure CO_2 as sweep gases at temperatures ranging from 800 to 1000 °C. In Fig. 5, temperature-dependent oxygen permeation fluxes of the newly developed NSAF–CN membranes (0.6 mm thick) are compared to those of NSF–CN membrane, previously reported by our group under the same conditions.[31] As can be seen in Fig. 5, partial substitution of Fe with Al has resulted in higher oxygen fluxes for NSAF6428–CN91 compared to NSF64–CN91 at all measured temperatures and with both He and CO_2 as sweep gases. This finding is in good agreement with previous studies conducted on perovskite membranes, which reported improved oxygen permeability and phase stability by limited Al doping in the Fe-sublattice.[49,51] At 950 °C, oxygen permeation fluxes of 0.26 and 0.21 $cm^3\ min^{-1}\ cm^{-2}$ were reported for NSF64–CN91 with He and CO_2, respectively, whereas the oxygen fluxes of 0.42 and 0.31 $cm^3\ min^{-1}\ cm^{-2}$ were measured on the NSAF6428–CN91 membrane at the same temperature and under the same conditions. The enhanced permeation fluxes of NSAF6428–CN91 can be attributed to various effects, such as increased concentration of oxygen vacancies as a result of lower average oxidation state of the B-site cations by partial substitution of Fe^{3+}/Fe^{4+} for Al^{3+}. Moreover, bulk diffusion of the oxygen ion is expected to be facilitated due to the higher symmetry of the cubic structure of the perovskite phase achieved by the introduction of smaller Al cation, as previously discussed. It should be noted, that the observed enhanced oxygen permeability of the Al-doped composition is substantially related to the initially higher oxygen non-stoichiometry, due to the lower average valence state of the Al-doped B-sublattice. According to Martynczuk *et al.*, Al^{3+} predominantly replaces Fe^{4+} at the B-sublattice rather than Fe^{3+}, which also enhances the effect of oxygen non-stoichiometry.[51] As shown in Fig. 6, the thermogravimetric analysis of the samples reveals that partial substitution of Fe for 20 at% Al does not significantly affect the thermally activated oxygen release from the lattice. Furthermore, increasing the amount of the acceptor dopant Sr^{2+}, results in a higher rate of reduction-induced oxygen release for NSAF5528–CN82.

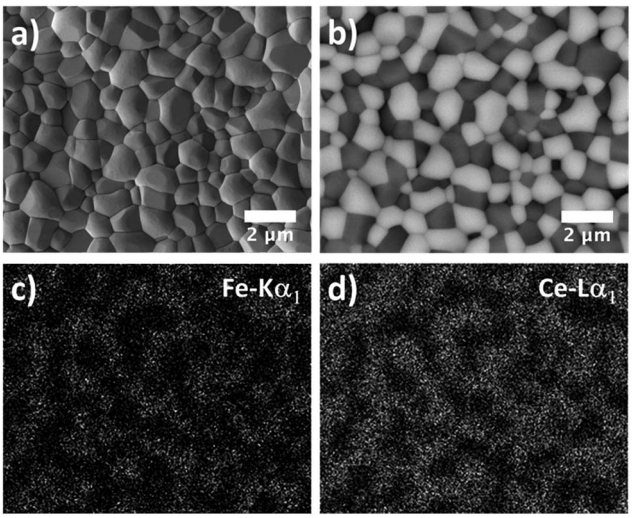

Fig. 3 Microstructure of NSAF6428–CN91 membrane sintered at 1400 °C for 5 h: (a) SEM micrograph, (b) BSEM micrograph, (c & d) elemental distribution of the area shown in panel (a) using EDXS analysis.

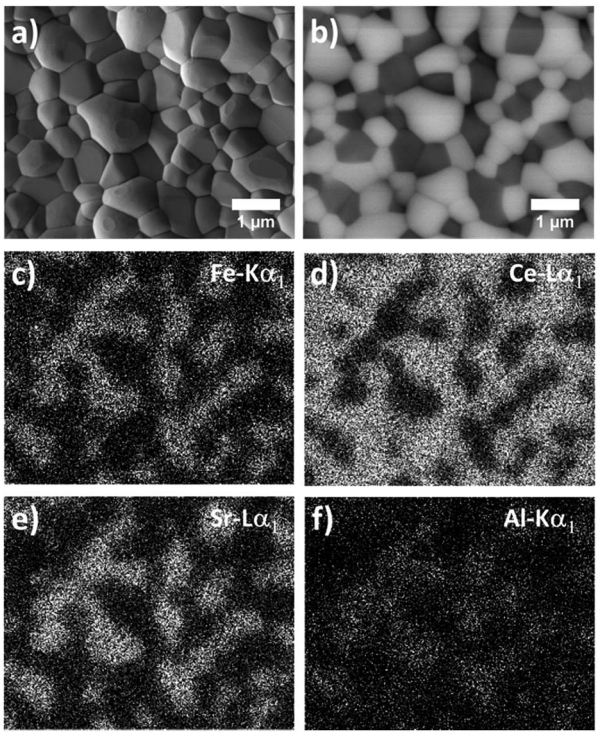

Fig. 4 Microstructure of NSAF5528–CN82 membrane sintered at 1400 °C for 5 h: (a) SEM micrograph, (b) BSEM micrograph, (c–f) elemental distribution of the area shown in panel (a) using EDXS analysis.

Published on 02 November 2015. Downloaded by Technische Informationsbibliothek (TIB) on 02/12/2016 07:36:39.

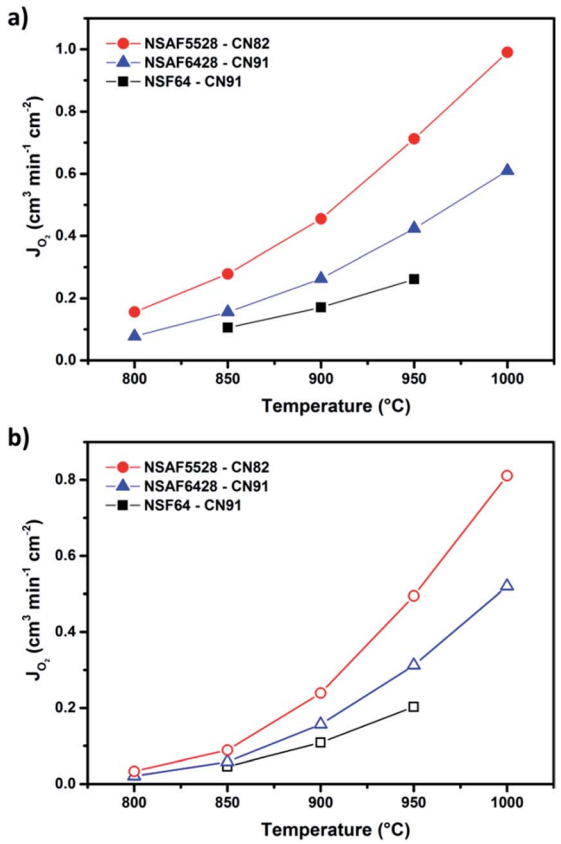

Fig. 5 Temperature-dependent oxygen permeation fluxes of NSAF–CN and NSF–CN[31] membranes with: (a) He as sweep gas (solid symbols), and (b) CO_2 as sweep gas (open symbols). Feed side: 150 cm^3 min^{-1} synthetic air. Sweep side: 49 cm^3 min^{-1} He (a) or CO_2 (b) +1 cm^3 min^{-1} Ne as internal standard. Membrane thickness: 0.6 mm.

In general, the overall oxygen permeation flux of a mixed-conducting membrane can be described by Wanger's theory of ambipolar conductivity.[52] Correspondingly, in a perovskite-type mixed ionic–electronic conductor, where the ionic conductivity is about two orders of magnitude lower than the electronic conductivity, the oxygen permeation flux is mainly controlled by the ionic conductivity. Therefore, a slight decrease in electrical conductivity has no significant effect on the overall oxygen permeation flux.

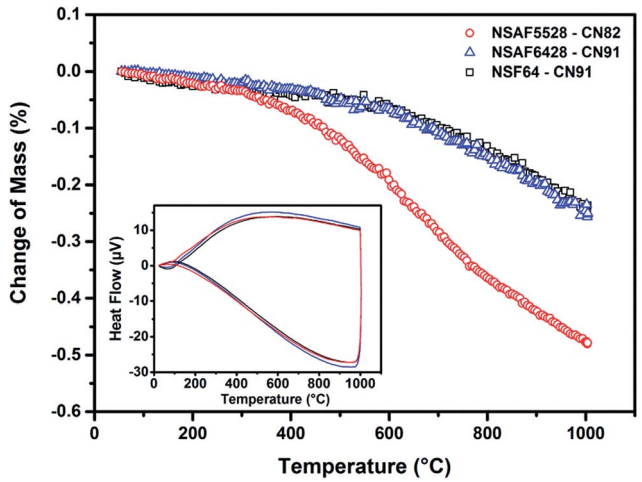

Fig. 6 TGA/DTA results of the dual-phase composites NSF–CN and NSAF–CN in synthetic air, flow of synthetic air: 20 cm^3 min^{-1}, heating/cooling rate: 10 °C min^{-1}. Inset: DTA results of the samples.

In summary, it can be concluded from the electrical conductivity results and the oxygen permeation measurements, that substitution of the B-site Fe for 20 at% Al has enhanced the oxygen permeability of the membrane at the cost of lower conductivity at temperatures above T_{max}, where the maximum electrical conductivity was observed.

Nevertheless, the highest oxygen permeation fluxes were observed for NSAF5528–CN82 with 0.71 and 0.50 cm^3 min^{-1} cm^{-2} at 950 °C with He and CO_2, respectively. The optimized oxygen permeability of NSAF5528–CN82 is attributed to increased oxygen non-stoichiometry in both fluorite and perovskite phases, resulted from 10 at% increase of Nd doping of the fluorite-type ceria and 10 at% higher Sr content at the A-site of the perovskite phase. However, increased amount of Sr could strongly compromise the CO_2 tolerance of the composition, as has been reported for single-phase perovskite membranes.[25,53,54] In order to investigate the effect of increased Sr content on the CO_2 stability of the membranes, long-term oxygen permeation tests were conducted on NSAF6428–CN91 and NSAF5528–CN82 membranes under air/CO_2 oxygen partial pressure gradients. The results of long-term oxygen permeation measurements under air/He and air/CO_2 gradients are shown in Fig. 7. Both membranes show stable oxygen fluxes under air/He oxygen partial pressure gradient at 1000 °C. The permeation fluxes under air/CO_2 oxygen partial pressure gradient display good long-term CO_2 stability at 1000 and 950 °C. An Ellingham diagram of collective data regarding thermodynamic stability of $SrCO_3$ in varying partial pressures of CO_2,[55] predicts a decomposition temperature of about 1084 °C (1357 K) under a CO_2 partial pressure of 1 atm. However, this consideration is based on the decomposition of pure $SrCO_3$ to SrO and CO_2. In case of Sr-containing perovskites, such as NSAF, lower decomposition temperature of $SrCO_3$ are expected, due to the negative stabilization energy of the perovskite structure,[56] and a high content of Nd at the A-site, that possesses higher stability against carbonate formation. The observation of stable oxygen fluxes at 1000 and 950 °C for CO_2-swept membranes is in accordance with the above statements. However, at 900 °C the NSAF6428–CN91 membrane with 10 at% lower content of Sr displays higher stability of oxygen fluxes in CO_2, compared to NSAF5528–CN82. For the NSAF6428–CN91 membrane stable oxygen fluxes of approx 0.15 cm^3 min^{-1} cm^{-2} were maintained for 100 h, whereas oxygen permeation fluxes of the NSAF5528–CN82 membrane gradually decreased from 0.24 to 0.19 cm^3 min^{-1} cm^{-2} in a 130 h course.

The phase composition of the membranes' feed and the sweep sides was studied using XRD. As can be seen in Fig. 8, the phase structures of both membranes were maintained after long-term permeation tests under air/CO_2 oxygen partial pressure gradients. The XRD analysis of the spent membranes

 This journal is © The Royal Society of Chemistry 2015

Published on 02 November 2015. Downloaded by Technische Informationsbibliothek (TIB) on 02/12/2016 07:36:39.

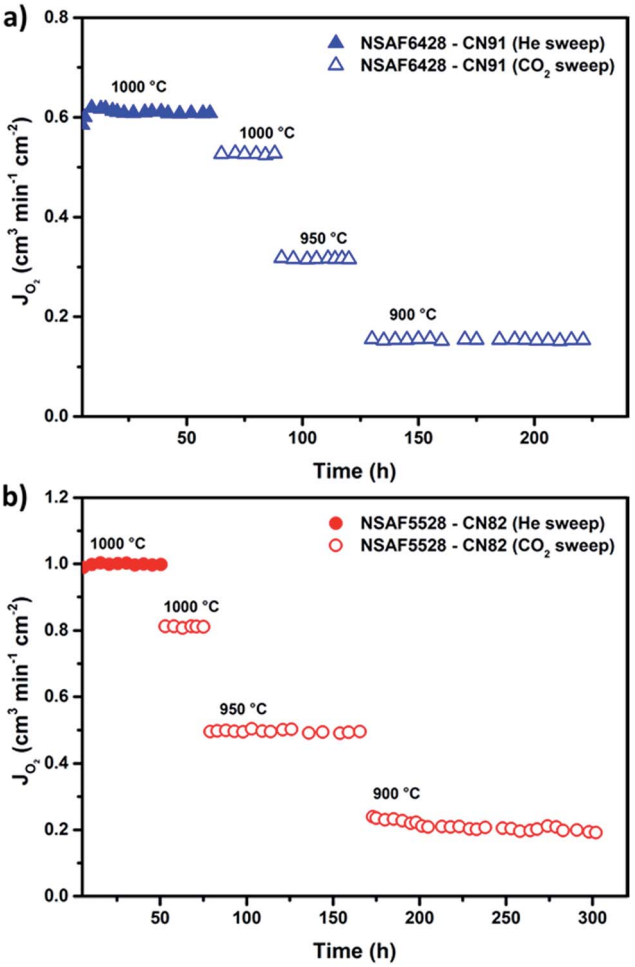

Fig. 7 Long-term oxygen permeation fluxes of: (a) NSAF6428–CN91, and (b) NSAF5528–CN82 membranes. Feed side: 150 cm^3 min^{-1} synthetic air. Sweep side: 49 cm^3 min^{-1} He (solid symbols) or CO_2 (open symbols) +1 cm^3 min^{-1} Ne as internal standard. Membrane thickness: 0.6 mm. (XRD and SEM of the membranes after permeation shown in Fig. 8 and 9).

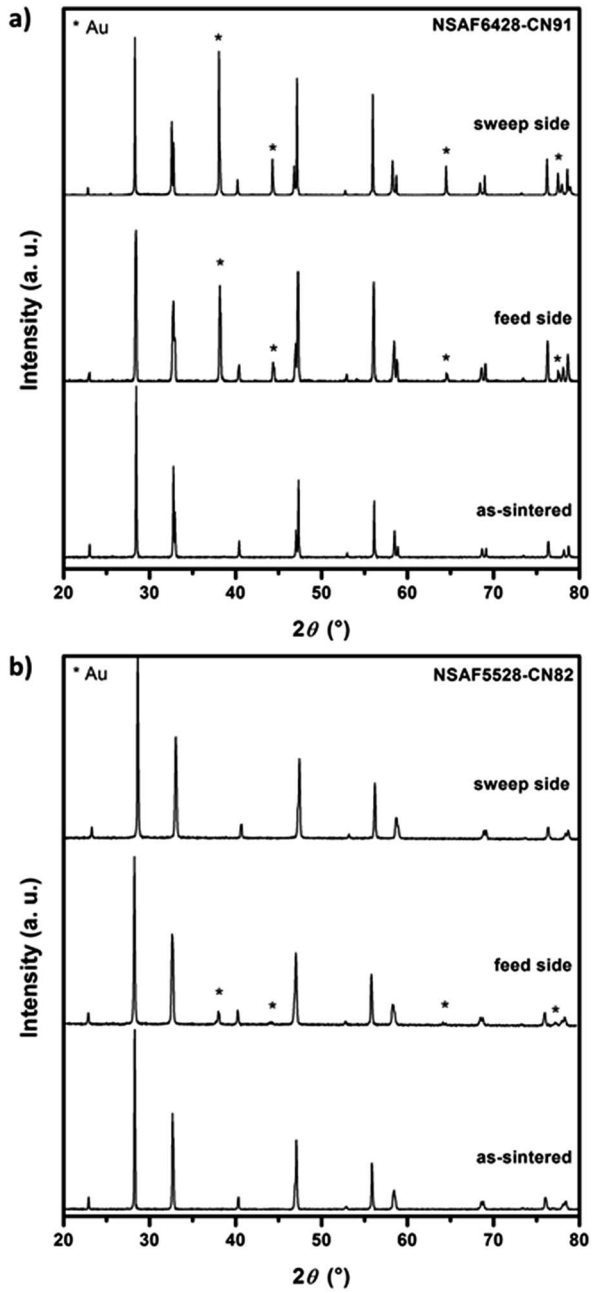

Fig. 8 Room temperature XRD patterns of: (a) NSAF6428–CN91, and (b) NSAF5528–CN82 membranes, as-sintered (bottom), the feed side (middle), and the sweep side (top) of the spent membrane after long-term permeation measurements (shown in Fig. 7). The reflection positions of gold originating from the sealing paste are marked with asterisk (*). (SEM images shown in Fig. 9).

revealed no evidence of any carbonate formation or other additional phases on the membranes surface, despite CO_2 exposures of >100 h for each membrane.

Subsequently, the microstructure of the spent membranes was analyzed using SEM. Fig. 9 shows the SEM micrographs of the feed and the sweep sides of the spent membranes. The microstructure of feed sides of both membranes was found to be unchanged and free of cracks or additional phases (Fig. 9a and c), which is in accordance with the XRD measurements shown in Fig. 8. On the CO_2-swept sides of both membranes (Fig. 9b and d), some superficial etching of the grains of the perovskite phase could be observed. In case of NSAF5528–CN82, the etching patterns were more significant, which is principally related to the formation of $SrCO_3$ at the lower temperature of 900 °C for a dwelling time of 130 h. Accordingly, the higher CO_2 reactivity of the NSAF5528–CN82 membrane material due to its higher Sr content explains the slight decrease in oxygen permeation flux of this membrane, shown in Fig. 7b. However, the SEM analysis of the cross-section of the spent NSAF5528–CN82 membrane, shown in Fig. 10, confirmed that the etching of the perovskite grains was limited to the surface layer of the membrane's CO_2-swept side and the integrity of the grains in the bulk was completely maintained. Consequently, the oxygen permeation flux is expected to reach a steady state, after the carbonate formation reaction ($Sr^{2+} + CO_3^{2-} \rightleftarrows SrCO_3$) is limited by a relative depletion of Sr from the surface layer of the perovskite grains.

Published on 02 November 2015. Downloaded by Technische Informationsbibliothek (TIB) on 02/12/2016 07:36:39.

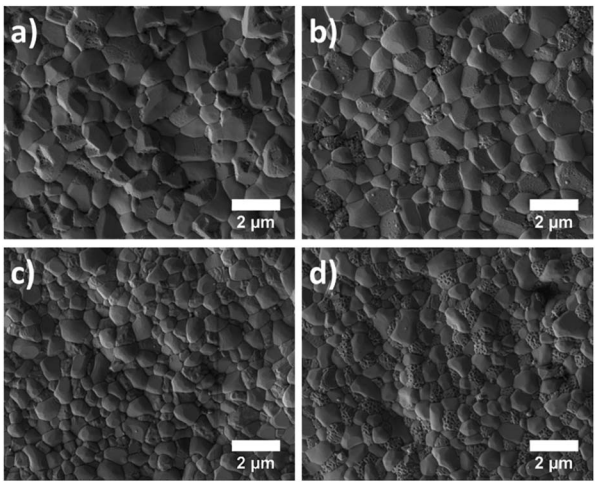

Fig. 9 SEM micrographs of the surface of the spent membranes after the permeation tests (shown in Fig. 7): (a) feed side of NSAF6428–CN91, (b) sweep side of NSAF6428–CN91, (c) feed side of NSAF5528–CN82, (d) sweep side of NSAF5528–CN82. (XRD patterns are shown in Fig. 8).

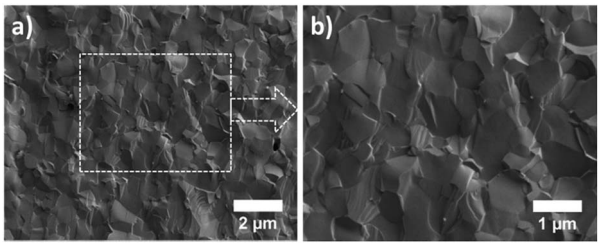

Fig. 10 SEM micrographs of NSAF5528–CN82 membrane cross-section after long-term permeation measurements under air/CO_2 oxygen partial pressure gradient (shown in Fig. 7): (a) packed grains close to the sweep side of the membrane, (b) magnification of area shown in (a).

Conclusions

The newly developed membranes NSAF6428–CN91 and NSAF5528–CN82 exhibited higher oxygen permeation fluxes compared to a similar composition containing only Fe at the B-site of the perovskite phase. Partial substitution of Fe^{3+}/Fe^{4+} for smaller Al^{3+} resulted in a higher oxygen vacancy concentration, due to the lower oxidation state of the B-site cations, and changed the crystal symmetry of the perovskite from orthorhombic to cubic at room temperature, thus facilitating isotropic bulk diffusion of the oxygen ions in the lattice.

Simultaneous increase in the perovskite's Sr content and the Nd doping of the fluorite phase resulted in higher oxygen permeation fluxes, due to increased oxygen non-stoichiometry. Both membranes showed very good long-term stability at 950 and 1000 °C, with pure CO_2 as the sweeping gas. At 900 °C, NSAF6428–CN91 showed a stable oxygen flux for 100 h under air/CO_2 oxygen partial pressure gradient, whereas NSAF5528–CN82 with 10 at% more Sr content exhibited a slight decrease in the permeation flux over 130 h. The SEM analysis of the surface of the membranes revealed no deterioration of the microstructure, apart from some minor etching patterns on the surface of the perovskite grains. In summary, the newly developed membranes showed high oxygen permeability and good CO_2 tolerance, for application in CO_2-rich environments, such as air separation units for CO_2 capture by oxyfuel concept.

Acknowledgements

The authors greatly acknowledge the financial support by DFG (Ca 147/18-1) and the Sino-German Centre for Research Promotion (GZ676 and GZ911). Prof. Dr C. H. Rüscher is gratefully acknowledged for the TGA/DTA measurements. Frank Steinbach is thanked for technical support.

Notes and references

1 H. J. M. Bouwmeester and A. J. Burggraaf, in *Fundamentals of Inorganic Membrane Science and Technology*, ed. A. J. Burggraaf and L. Cot, Elsevier Science B. V., Amsterdam, The Netherlands, 1996, ch. 10, pp. 435–528.
2 U. Balachandran, B. Ma, P. S. Maiya, R. L. Mieville, J. T. Dusek, J. J. Picciolo, J. Guan, S. E. Dorris and M. Liu, *Solid State Ionics*, 1998, **108**, 363.
3 F. Y. Liang and J. Caro, in *Membrane Engineering for the Treatment of Gases*, ed. E. Drioli and G. Barbieri, Royal Society of Chemistry, 2011, vol. 2, pp. 192–221.
4 J. E. ten Elshof, H. J. M. Bouwmeester and H. Verweij, *Appl. Catal., A*, 1995, **130**, 195.
5 J. Caro, K. J. Caspary, C. Hamel, B. Hoting, P. Koelsch, B. Langanke, K. Nassauer, T. Schiestel, A. Schmidt, R. Schomaecker, A. Seidel-Morgenstern, E. Tsotsas, I. Voigt, H. H. Wang, R. Warsitz, S. Werth and A. Wolf, *Ind. Eng. Chem. Res.*, 2007, **46**, 2286.
6 H. Q. Jiang, Z. W. Cao, S. Schirrmeister, T. Schiestel and J. Caro, *Angew. Chem., Int. Ed.*, 2010, **49**, 5656.
7 X. F. Zhu, Q. Li, Y. He, Y. Cong and W. Yang, *J. Membr. Sci.*, 2010, **360**, 454.
8 H. H. Wang, C. Tablet, T. Schiestel, S. Werth and J. Caro, *Catal. Commun.*, 2006, **7**, 907.
9 Z. P. Shao and S. M. Haile, *Nature*, 2004, **431**, 170.
10 K. Huang, J. Wan and J. B. Goodenough, *J. Mater. Sci.*, 2001, **36**, 1093.
11 X. Tan, K. Li, A. Thursfield and I. S. Metcalfe, *Catal. Today*, 2008, **131**, 292.
12 Q. Zeng, Y. B. Zuo, C. G. Fan and C. S. Chen, *J. Membr. Sci.*, 2009, **335**, 140.
13 N. MacDowell, N. Florin, A. Buchard, J. Hallett, A. Galindo, G. Jackson, C. S. Adjiman, C. K. Williams, N. Shah and P. Fennell, *Energy Environ. Sci.*, 2010, **3**, 1645.
14 P. Markewitz, W. Kuckshinrichs, W. Leitner, J. Linssen, P. Zapp, R. Bongartz, A. Schreiber and T. E. Müller, *Energy Environ. Sci.*, 2012, **5**, 7281.
15 R. S. Haszeldine, *Science*, 2009, **325**, 1647.
16 M. Schulz, R. Kriegel and A. Kämpfer, *J. Membr. Sci.*, 2011, **378**, 10.

 This journal is © The Royal Society of Chemistry 2015

Published on 02 November 2015. Downloaded by Technische Informationsbibliothek (TIB) on 02/12/2016 07:36:39.

17 Y. Teraoka, H. M. Zhang and N. Yamazoe, *Chem. Lett.*, 1985, 1367.
18 J. F. Vente, S. McIntosh, W. G. Haije and H. J. M. Bouwmeester, *J. Solid State Electrochem.*, 2006, **10**, 581.
19 Z. P. Shao, W. S. Yang, Y. Cong, H. Dong, J. H. Tong and G. X. Xiong, *J. Membr. Sci.*, 2000, **172**, 177.
20 S. Baumann, J. M. Serra, M. P. Lobera, S. Escolástico, F. Schulze-Küppers and W. A. Meulenberg, *J. Membr. Sci.*, 2011, **377**, 198.
21 J. M. Serra, V. B. Vert, M. Betz, V. A. C. Haanappel, W. A. Meulenberg and F. Tietz, *J. Electrochem. Soc.*, 2008, **155**, B207.
22 K. Partovi, B. Geppert, F. Y. Liang, C. H. Rüscher and J. Caro, *Chem. Mater.*, 2015, **27**, 2911.
23 X. Tan, N. Liu, B. Meng, J. Sunarso, K. Zhang and S. Liu, *J. Membr. Sci.*, 2012, **389**, 216.
24 A. Waindich, A. Mobius and M. Müller, *J. Membr. Sci.*, 2009, **337**, 182.
25 M. Arnold, H. H. Wang and A. Feldhoff, *J. Membr. Sci.*, 2007, **293**, 44.
26 O. Czuprat, M. Arnold, S. Schirrmeister, T. Schiestel and J. Caro, *J. Membr. Sci.*, 2010, **364**, 132.
27 X. F. Zhu, H. Liu, Y. Cong and W. Yang, *Chem. Commun.*, 2012, **48**, 251.
28 Z. Wang, W. Sun, Z. Zhu, T. Liu and W. Liu, *ACS Appl. Mater. Interfaces*, 2013, **5**, 11038.
29 H. X. Luo, H. Q. Jiang, T. Klande, Z. W. Cao, F. Y. Liang, H. H. Wang and J. Caro, *Chem. Mater.*, 2012, **24**, 2148.
30 F. Y. Liang, H. X. Luo, K. Partovi, O. Ravkina, Z. W. Cao, L. Yi and J. Caro, *Chem. Commun.*, 2014, **50**, 2451.
31 H. X. Luo, T. Klande, Z. W. Cao, F. Y. Liang, H. H. Wang and J. Caro, *J. Mater. Chem. A*, 2014, **2**, 7780.
32 Z. Wu, W. Jin and N. Xu, *J. Membr. Sci.*, 2006, **279**, 320.
33 X. Zhu, Q. Li, Y. Cong and W. Yang, *Catal. Commun.*, 2008, **10**, 309.
34 X. Dong, Z. Xu, X. Chang, C. Zhang and W. Jin, *J. Am. Ceram. Soc.*, 2007, **90**, 3923.
35 A. L. Shaula, V. V. Kharton, N. P. Vyshatko, E. V. Tsipis, M. V. Patrakeev, F. M. B. Marques and J. R. Frade, *J. Eur. Ceram. Soc.*, 2005, **25**, 489.
36 F. Y. Liang, K. Partovi, H. Q. Jiang, H. X. Luo and J. Caro, *J. Mater. Chem. A*, 2013, **1**, 746.
37 A. Feldhoff, M. Arnold, J. Martynczuk, T. M. Gesing and H. Wang, *Solid State Sci.*, 2008, **10**, 689.
38 M. Arnold, H. Wang, J. Martynczuk and A. Feldhoff, *J. Am. Ceram. Soc.*, 2007, **90**, 3651.
39 X. Zhu, H. Wang and W. Yang, *J. Membr. Sci.*, 2008, **309**, 120.
40 K. Partovi, F. Y. Liang, O. Ravkina and J. Caro, *ACS Appl. Mater. Interfaces*, 2014, **6**, 10274.
41 J. L. Garcia-Munoz and J. Rodriguez-Carvajal, *Phys. Rev. B: Condens. Matter Mater. Phys.*, 1992, **46**, 4414.
42 V. M. Goldschmidt, *Skr. Nor. Viedenk.-Akad., Kl. I: Mater.-Naturvidensk. Kl.*, 1926, 8.
43 R. D. Shannon, *Acta Crystallogr., Sect. A: Cryst. Phys., Diffr., Theor. Gen. Crystallogr.*, 1976, **32**, 751.
44 J. W. Stevenson, T. R. Armstrong, R. D. Carneim, L. R. Pederson and W. J. Weber, *J. Electrochem. Soc.*, 1996, **143**, 2722.
45 L. W. Tai, M. M. Nasrallah, H. U. Anderson, D. M. Sparlin and S. R. Sehlin, *Solid State Ionics*, 1995, **76**, 259.
46 S. Sekido, H. Tachibana, Y. Yamamura and T. Kambara, *Solid State Ionics*, 1990, **37**, 253.
47 J. E. ten Elshof, H. J. M. Bouwmeester and H. Verweij, *Solid State Ionics*, 1995, **81**, 97.
48 J. Holc, D. Kuscer, M. Hrovat, S. Bernik and D. Kolar, *Solid State Ionics*, 1997, **95**, 259.
49 V. V. Kharton, A. L. Shaula, F. M. M. Snijkers, J. F. C. Cooymans, J. J. Luyten, A. A. Yaremchenko, A. A. Valente, E. V. Tsipis, J. R. Frade, F. M. B. Marques and J. Rocha, *J. Membr. Sci.*, 2005, **252**, 215.
50 L. W. Tai, M. M. Nasrallah, H. U. Anderson, D. M. Sparlin and S. R. Sehlin, *Solid State Ionics*, 1995, **76**, 273.
51 J. Martynczuk, F. Y. Liang, M. Arnold, V. Sepelak and A. Feldhoff, *Chem. Mater.*, 2009, **21**, 1568.
52 C. Wagner, *Prog. Solid State Chem.*, 1975, **10**, 3.
53 T. Klande, O. Ravkina and A. Feldhoff, *J. Membr. Sci.*, 2013, **437**, 122.
54 O. Ravkina, T. Klande and A. Feldhoff, *J. Membr. Sci.*, 2015, **480**, 31.
55 K. Efimov, T. Klande, N. Juditzki and A. Feldhoff, *J. Membr. Sci.*, 2012, **389**, 205.
56 H. Yokokawa, N. Sakai, T. Kawada and M. Dokiya, *Solid State Ionics*, 1992, **52**, 43.